Chemical Science

ROYAL SOCIETY OF CHEMISTRY

EDGE ARTICLE

View Article Online
View Journal

Cite this: DOI: 10.1039/d5sc06475a

All publication charges for this article have been paid for by the Royal Society of Chemistry

Unprecedented HAT rate acceleration in water by a non-heme manganese oxo complex

Puja De,[a] Snehith Adabala,[b] Soumya Samanta,[c] Kuntal Mukhopadhyay,[a] Soumya Ghosh *[b] and Sayam Sen Gupta *[a]

Received 24th August 2025
Accepted 17th December 2025

DOI: 10.1039/d5sc06475a

rsc.li/chemical-science

Nature employs water as the reaction medium for enzymatic redox transformations, taking advantage of its unique physicochemical properties to precisely regulate reaction kinetics, selectivity, and proton-coupled electron transfer. In a biomimetic endeavour, using a newly developed non-heme $(Et_4N)[Mn^{V}(O)(Ph,Me\text{-}bTAML)]$ complex, we report a water-induced, enzyme-like rate acceleration in hydrogen atom transfer (HAT) reactivity with various substrates possessing BDEs of 67–78 kcal mol^{-1}. In acetonitrile, the reactivity is sluggish, but switching to water – particularly beyond 85% content – results in a dramatic rate enhancement, peaking in pure water with up to a 20 000-fold increase. This effect occurs without any structural changes or addition of external additives. Mechanistic insights suggest that water stabilises the minimum energy crossing point (MECP) more effectively than acetonitrile through enhanced electrostatics and hydrogen bonding in transition-state energetics. This is the first demonstration of a non-heme Mn(V)-oxo complex mimicking enzymatic rate enhancement solely *via* solvent modulation. The work highlights water's active role in driving selective, efficient, and green oxidation chemistry, unlocking new potential in bioinspired catalysis.

Introduction

Water acts as a safe, non-toxic, inexpensive, and environmentally benign alternative reaction medium for a broad range of organic transformations.[1] Green chemistry emphasises the use of water as an environmentally benign, non-toxic, and renewable solvent to replace hazardous organic solvents, thereby reducing pollution and enhancing sustainability in chemical processes.[2] In addition, seminal work by Breslow *et al.* in the 1980s has shown that water can enhance reaction rates and greater selectivity compared to classical organic solvents.[3,4] Nature harnesses the distinctive physical and chemical properties of water to control the rate, selectivity, and mass-transfer dynamics of enzymatic reactions by stabilising reactive intermediates through hydrogen bonding and enabling efficient proton-transfer pathways.[5–8] Although these reactions take place in an aqueous environment, they are primarily influenced not by the bulk properties of water but by the hydrophobic pocket of the globular protein surrounding the active site.[9–12] However, in certain enzymatic systems, such as in the oxidation of chromopyrrolic acid (CPA) by cytochrome P450 StaP, a structured, confined water network forms within the hydrophobic pocket near the redox-active centre, playing a crucial role in modulating electron and proton transfer processes.[13]

Beyond biology, water has become a sustainable solvent that replaces toxic organics while reducing pollution and improving reaction efficiency.[14] Previously, it was found that many pericyclic reactions, such as Diels–Alder cycloadditions and Claisen rearrangements of organic compounds, were accelerated in an aqueous medium.[15] In 2005 K. Barry Sharpless reported the cycloaddition reaction between DMAD and quadricyclane under 'on water' conditions, which shows a high-rate acceleration under ambient conditions than in different polar and non-polar organic media (even under neat conditions).[16] The accelerated rates of organic reactions in aqueous environments, particularly in "on-water" mechanisms, arise from several key factors such as the hydrophobic effect and solvophobicity, stabilisation of transition states through hydrogen bonding, and high cohesive energy density.[17,18] The partial polarisation at the solvent–solute interface due to sudden exchange of protons *via* the grotthus mechanism, would place the reactants and catalysts in definite orientations, forming highly oriented transition states, which also favour the high rate acceleration.[3,19] These characteristics underline water's pivotal role as an environmentally friendly solvent, enhancing the reactivity of organic and inorganic compounds in an aqueous suspension.

Sen Gupta and co-workers developed novel catalysts with a biuret tetra-amido macrocyclic ligand (bTAML), capable of performing challenging oxidative organic transformations and catalytic water oxidation in organic solvents (CH_3CN) by

[a]Department of Chemical Sciences, Indian Institute of Science Education and Research, Mohanpur, Kolkata, 741246, India. E-mail: sayam.sengupta@iiserkol.ac.in
[b]Tata Institute of Fundamental Research Hyderabad, Hyderabad, Telangana 500046, India. E-mail: soumya.ghosh@tifrh.res.in
[c]School of Chemical Sciences Indian Association for the Cultivation of Science, Kolkata, West Bengal 700032, India

stabilising an Fe(V)-oxo intermediate at room temperature.[20–26] In 2023, they introduced a modified complex, $(Et_4N)_2$[-Fe(Cl)(Ph,Me-bTAML)], which enables regio and stereo-retentive oxidation of unactivated C–H bonds in 100% water using H_2O_2 effectively mimicking the cytochrome P450 enzymes.[25] The proposed Fe(V)-oxo intermediate for this reaction was successfully trapped in water using *m*CPBA, exhibiting a half-life ($t_{1/2}$) of approximately 6 seconds at 298 K. Interestingly, in pure water, the intermediate demonstrated nearly 300 times higher reactivity toward the 6-methylheptan-2-yl isonicotinate substrate compared to its behaviour in acetonitrile.[25] The remarkable rate enhancement observed for the high-valent Fe(V)-oxo complexes naturally sparks a strong sense of curiosity to explore the role of water in driving such extraordinary reactivity. However, despite these advancements, the instability of the Fe(V)-oxo intermediate in pure water posed significant challenges, limiting a comprehensive investigation of its thermodynamic and kinetic properties. This limitation redirected attention toward manganese-based complexes, which offer a more stable Mn(V)-oxo intermediate,[27] paving the way for further exploration and breakthroughs. By treating $[Et_4N]_2$[-Mn^{III}(Cl)(Ph,Me-bTAML)] with iodosyl benzene or NaOCl, a high-valent Mn(V)-oxo complex was generated, demonstrating a dramatic change in kinetic properties in changing the solvent from acetonitrile to water. The Mn(V)-oxo complex showed an astonishing up to twenty-thousand-fold rate increase in hydrogen atom transfer (HAT) reactions in water compared to organic solvent, CH_3CN. This dramatic rate enhancement was attributed to favourable activation enthalpy and a structured transition state enabled by water's hydrogen-bonding network. Our results highlight the unique potential of Mn-oxo complexes for efficient C–H bond oxidation in aqueous media. To the best of our knowledge, this work represents the first demonstration of such a remarkable HAT rate enhancement in pure water using a non-heme metal-oxo complex. Importantly, this acceleration was achieved without any structural modification of the complex or the involvement of redox-active/inactive metal ions, Lewis acids, or Brønsted acids—arising solely from solvent modulation.[28–37] This finding underscores a greener and more sustainable approach for tuning reactivity in bioinspired oxidation chemistry.

Results and discussion

Generation and characterisation of $(Et_4N)[Mn^V(O)$(Ph,Me-bTAML)], 2

The (Ph,Me-bTAML) ligand was synthesised by following the previously reported procedure.[25] A new Mn-bTAML complex $[Et_4N]_2[Mn^{III}(Cl)$(Ph,Me-bTAML)], **1**, was synthesised by mixing an excess amount of anhydrous $MnCl_2$ with the solution of ligand (Ph,Me-bTAML) and *n*-BuLi in THF at 0 °C (detailed procedure is described in the SI, Experimental results Section 4A). The resulting complex was purified and subsequently characterised by UV-vis, ESI-MS (Fig. 2A and S1) and X-ray crystallography (Fig. 1). Treatment of **1** with 1.5 equiv. of iodosylbenzene (PhIO) or NaOCl, either in 100% CH_3CN or water (or mixtures of CH_3CN-water) under ambient conditions (d^2

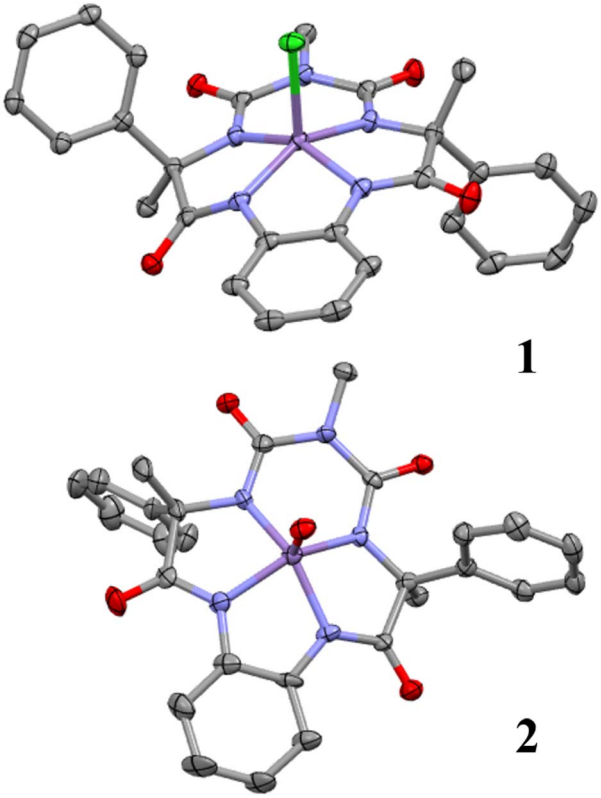

Fig. 1 X-ray crystal structures of both **1** and **2** with ellipsoid probability 50% and 40% respectively (hydrogens, solvent molecules, and tetraethyl ammonium molecules are omitted for clarity).

system, diamagnetic confirmed by EPR and NMR, Fig. S7 and S8) generated a nonheme Mn(V)-oxo complex, **2**, which was highly stable at room temperature in both solvents (Scheme 1). High stability of the complex allowed us to characterise this using single crystal X-ray crystallography (Fig. 1, see the SI, Experimental results Section 4B) and various other spectroscopic techniques. The UV-vis absorption spectrum of this Mn(V)-oxo complex displayed a λ_{max} of 442 nm (ε = 4500 M^{-1} cm^{-1}) in 100% CH_3CN and 432 nm in 100% water (Fig. 2A). HRMS of **2** in negative mode, in both CH_3CN and a water medium, exhibited a major peak at m/z = 552.1038 corresponding to the formation of $[Mn^V(O)$(Ph,Me-bTAML)]$^-$ [calculated m/z = 552.11] (Fig. 2B). When **2** was stirred in H_2O^{18}, a mass peak corresponding to $[Mn^V(^{18}O)$(Ph,Me-bTAML)]$^-$ (~27%) appeared at m/z = 554.0855 [calculated m/z = 554.11], along with the mass peak of $[Mn^V(O)$(Ph,Me-bTAML)]$^-$ (Fig. 2B). The short Mn–O bond length of 1.556(7) Å in the X-ray crystal structure of **2** (Fig. 1; see SI Tables S7 and S8) is consistent with the Mn–O triple bond character. The Raman spectrum of complex **2** obtained upon excitation at 488 nm at room temperature, revealed a single isotopically sensitive band for Mn–O stretch at 979 cm^{-1} in water, which shifted to 939 cm^{-1} upon using H_2O^{18} (Fig. S5). The observed isotopic shift of 40 cm^{-1} upon ^{18}O labelling was consistent with the predicted shift of the Mn–O stretch using Hooke's law, confirming the presence of a triple Mn–O bond character.[27] Single crystal X-ray

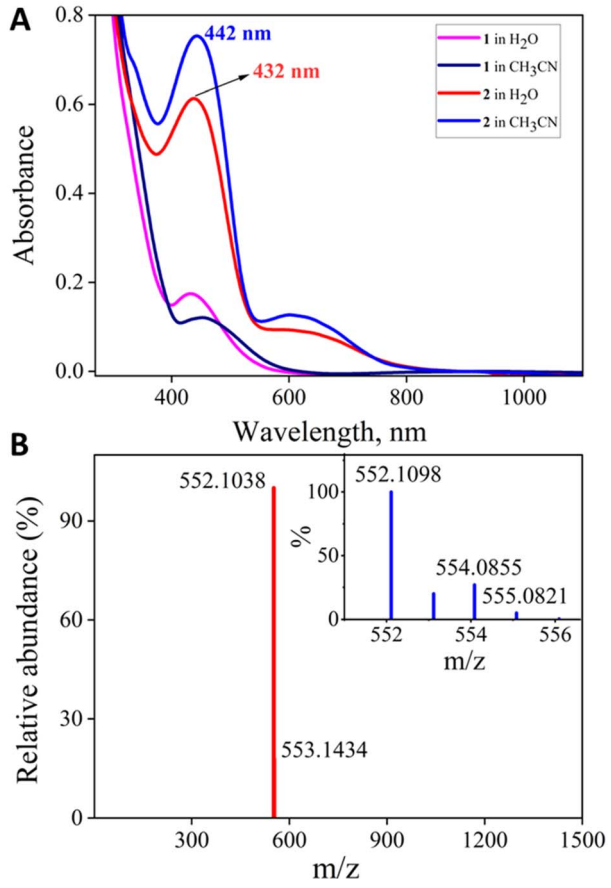

Fig. 2 (A) UV-vis spectra of **2**, both in 100% CH_3CN and water from **1** at RT. (B) Negative mode HRMS spectrum of **2** (0.05 mM) in water and mass spectrum of **2** in H_2O^{18} (inset).

studies indicate that Mn exhibits a slightly distorted square-pyramidal geometry, which arises from the axial oxo ligand and the four amido-N ligands (Mn–N average distance of 1.8645 Å). Taken together, **2** is a low-spin ($S = 0$) Mn(V)-oxo complex with Mn–O triple bond character.

Reactivity studies of 2 towards C–H bonds and a mechanistic investigation

The HAT reactivity of **2** was investigated with a range of C–H bond substrates in both CH_3CN and water. To compare second-order reaction rates, a common substrate soluble in both solvents was selected. 1-Benzyl-1,4-dihydronicotinamide (BNAH) was chosen as the primary substrate for these comparative studies in aqueous media owing to its solubility

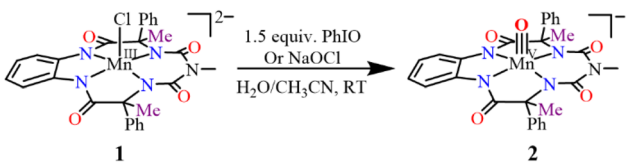

Scheme 1 Schematic diagram for the synthesis of complex (Et_4N) $[Mn^V(O)(Ph,Me\text{-}bTAML)]$, **2** from **1**.

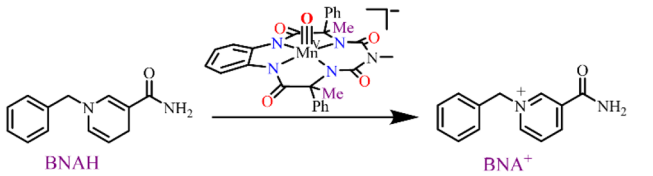

Scheme 2 Schematic diagram for the reaction of **2** (0.05 mM) with BNAH.

(Scheme 2). This property enabled the investigation of pseudo-first-order kinetics under homogeneous conditions. The addition of BNAH to a solution containing **2** in CH_3CN led to a very slow decay of the characteristic UV-vis peak at 442 nm, which enabled us to obtain the pseudo-first-order rate constants over the temperature range of 333–303 K (Fig. S11 and S14). At 293 K, the kinetics of this reaction was very slow to reliably determine pseudo-first-order rate constants. Notably, the Mn(V)-oxo species remained stable even at these elevated temperatures, ensuring the absence of any background rates (Fig. S4). In contrast, a very rapid decay of the characteristic UV-vis peak at 432 nm was observed when the same reaction was carried out in 100% water at 293 K (Fig. S11). The second-order rate constants (k_2) were subsequently determined by plotting the pseudo-first-

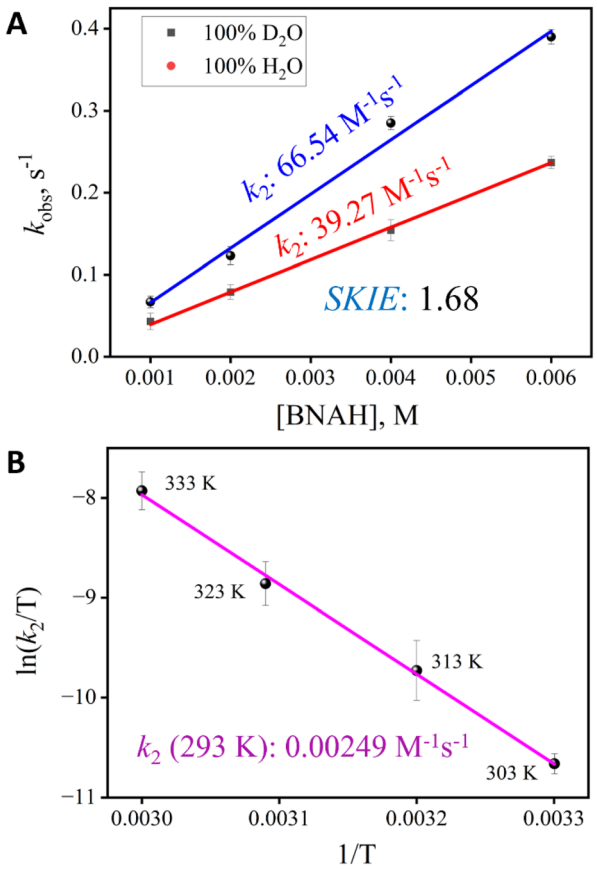

Fig. 3 (A) Plot of the k_2 value for the reaction of **2** (0.05 mM) with varying [BNAH] at 293 K, in H_2O and D_2O, to determine the solvent kinetic isotope effect. (B) Determination of k_2 at 293 K for reaction of **2** (0.05 mM) with BNAH in pure acetonitrile solvent from the Eyring plot.

order rate constants (k_{obs}) as a function of the relative increase in the substrate concentration at 293 K (Fig. 3A and S17). In both H_2O and CH_3CN, the reaction of complex **2** with BNAH formed BNA^+ with the concomitant regeneration of complex **1** (detected *via* water HRMS, Fig. S31 and S32). To compare the reactivity of complex **2** with BNAH in both CH_3CN and H_2O, we chose 293 K as the temperature, since at temperatures of 303 K and above, the reactivity in 100% water was too fast for reliable determination of k_2. The k_2 value for the reaction in 100% CH_3CN at 293 K was therefore obtained by extrapolating the linear Eyring plot to 293 K (Fig. 3B). Remarkably, the reaction of compound **2** with BNAH was 26 700 times faster in water than in CH_3CN at 293 K. The kinetic investigation using BNAH was also carried out in deuterated water to determine the SKIE value. The SKIE value of 1.68 (Fig. 3A), which was corrected by taking into account both the concentrations of water and deuterated water,[38] indicates the stabilisation of the transition state with the hydrogen bonding network. Kinetic studies of **2** with BNAH were also carried out in different CH_3CN–water mixtures to understand the impact of increasing the water concentration at 293 K (Fig. S12 and S13). Remarkably, the rate enhancement occurs exponentially from 80% water, and saturates at 95% giving a sigmoidal curve (Fig. 4). This indicates that a particular water concentration (≥90%) was required for such a large rate acceleration.

In addition to BNAH (67 kcal mol^{-1}), the comparison of HAT reactivity in both media towards different C–H bond substrates, including 9,10-dihydroacridine ($ACrH_2$) (72 kcal mol^{-1}), xanthene (75.5 kcal mol^{-1}), and 9,10-dihydroanthracene (DHA) (78 kcal mol^{-1}), was also studied at room temperature.[39–41] Product formation was detected by GC-MS under single turnover conditions (Table S9). These substrates span a narrow range of C–H bond dissociation energies (BDE_{C-H}) from 70 to 78 kcal mol^{-1} and hence should elucidate the thermodynamics behind the HAT reaction rates by **2**. Next, we plotted the natural logarithm of the initial rate constants (Fig. S21) [initial rates are calculated by checking the formation of product concentration using GC-MS at different time intervals] for HAT by **2** *versus* the BDE_{C-H} of the substrates (Fig. S20, S22–S25, Table 1). The linearity and the nonzero slope value of the Bell–Evans–Polanyi plot ($\log k_2$ *versus* BDE_{C-H}) gives evidence of a rate-determining step involving the hydrogen atom abstraction reaction (Fig. S21). Again, in water, the reaction rates of **2** with 9,10-dihydroacridine, xanthene, and 9,10-dihydroanthracene increased remarkably, reaching values 3500, 4700, and 5000 times higher, respectively, than those observed in an acetonitrile medium (Table 1, SI Table S11).

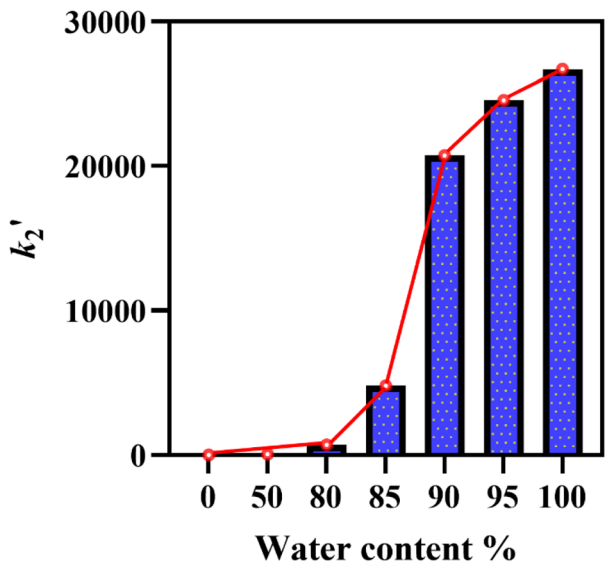

Fig. 4 Graphical representation of relative second-order rate constant values (k_2') for the reaction of **2** (0.05 mM) with BNAH at 293 K at different water ratios where $k_2' = k_2$, H_2O/k_2, CH_3CN.

Table 1 Determination of the rate enhancement factor (k') for complex **2** with different C–H bond substrates in both solvents at RT. Relative rates (k') were determined either from second-order rate constants (a) or from initial rate constant values (b)

	Substrates			
	[a]BNAH	[b]9,10 $AcrH_2$	[b]Xanthene	[b]9,10 DHA
k' (k_{H_2O}/k_{CH_3CN})	26 700	3500	4700	5000

To gain further insight into the reaction mechanism, the HAT of BNAH-4,4′-d_2 with **2** was studied, and a KIE of 11 was obtained (Fig. S28). The process of hydrogen atom abstraction generally involves the simultaneous transfer of a proton and electron. The 10^4-fold acceleration in reactivity, compared to other C–H bond substrates (10^3-fold), can be attributed to the redox potential of BNAH being less than 1 V.[42] This value closely aligns with the redox potential of complex **2**, facilitating a reaction primarily driven by asynchronous electron transfer–proton transfer (ET–PT).[43] However, a significant KIE implies that the proton transfer plays a significant role in determining the rate of oxidation of C–H bonds by **2** which is consistent with the earlier report.[44] The reaction of BNAH with **2** accelerates by a factor of 1.64 when lithium chloride is added to the aqueous solvent, while it decelerates by a factor of 4.59 upon the addition of guanidinium chloride (Fig. S19 and S29). This observation highlights the role of the Breslow hydrophobic effect as a contributing factor to the rate enhancement observed when transitioning to water from organic solvent.[18]

Determination of thermodynamic parameters for BNAH oxidation with 2

For a better understanding of the transition state, variable-temperature kinetic measurements were carried out for BNAH oxidation to determine the activation parameters (Fig. 3B and S16) on the basis of Eyring plots for the rate constants. According to the activation parameters for BNAH oxidation with **2** in CH_3CN ($\Delta H^{\#} = 17.81$ kcal mol^{-1}; $T\Delta S^{\#} = -2.80$ kcal mol^{-1}; 293 K) and 100% H_2O ($\Delta H^{\#} = 7.53$ kcal mol^{-1}; $T\Delta S^{\#} = -7.26$ kcal mol^{-1}; 293 K), the twenty-thousand-fold increase in the reaction rate is mainly governed by the favourable activation enthalpy terms (a gain of 10.27 kcal mol^{-1} in $\Delta H^{\#}$). In contrast, the contribution of the activation entropy (as a loss of

4.46 kcal mol^{-1} in $\Delta S^{\#}$) to the transition state is negative in water. Because the enthalpy gain is 2.30 times greater than the entropic loss, a favourable Gibbs energy of activation, $\Delta G^{\#}$, leads to rate acceleration in water. The gain in enthalpy with a concomitant loss in entropy indicates the formation of an ordered transition state involving water molecules.

Understanding the perturbation of redox potential and pK_a with a change in solvent

The dramatic change in reactivity upon switching the solvent from CH_3CN to water may stem from changes in the pK_a of the "oxo" group in the Mn(V)-oxo or the shift in the Mn(IV)/Mn(V) redox potential. To probe this, Raman spectroscopy was employed to monitor the Mn–O stretch, which can be a reflection of its pK_a, in both solvents. Upon excitation at 413 nm at 78 K, **2** revealed a Mn–O stretching vibration at 973 cm^{-1} in CH_3CN, which shifted slightly to 979 cm^{-1} in water (Fig. S5). This minor shift upon switching the solvent to water suggests that changes in pK_a are unlikely to drive the observed increase in HAT reactivity in water.

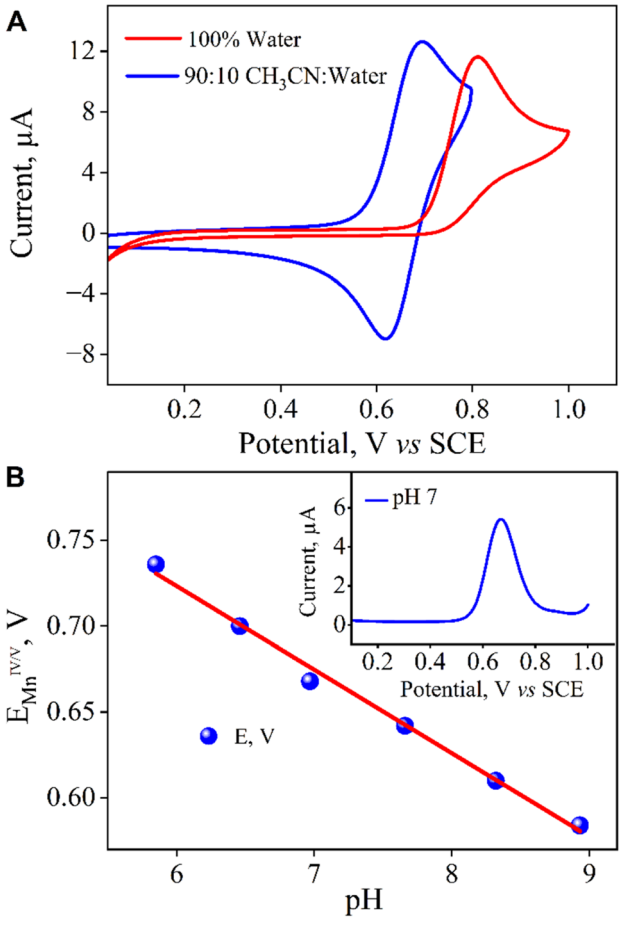

Fig. 5 (A) CV of **1** (0.5 mM) both in 9 : 1 CH_3CN : H_2O and 100% water using glassy carbon as the working electrode and a Pt wire as the counter electrode at RT (scan towards the positive direction). (B) Plot of Mn(IV)/Mn(V) redox potential *vs.* pH in water with a slope of 49 mV per unit, indicating a 1H$^+$/1e$^-$ PCET process; inset shows DPV data of **1**.

Next, the redox behaviour of complex **1** was evaluated by cyclic voltammetry (CV) in both 9 : 1 CH_3CN : H_2O and 100% water, using a glassy carbon working electrode and a platinum wire counter electrode (Fig. 5A). In H_2O, a quasi-reversible one-electron wave at $E_{1/2}$ = 0.76 V *vs.* SCE was observed by cyclic voltammetry. Controlled-potential electrolysis (CPE) performed at 0.8 V *vs.* SCE led to the formation of the dark green Mn(V)-oxo that fully resembled **2** (Fig. S9). Furthermore, differential pulse voltammetry (DPV) in water revealed a pH-dependent shift in this redox couple with a slope of 49 mV per pH unit (Fig. 5B), indicative of a proton-coupled electron transfer (PCET) process involving 1H$^+$/1e$^-$.[45–47] This led us to conclude that in 100% water, this feature in CV corresponds to the $Mn^{V}(O)/Mn^{IV}(OH)$ couple (see eqn (2) below). Similarly, the Mn(III/IV) couple was detected using a gold working electrode[48] and exhibited the same pH dependence (49 mV per pH unit), further supporting the involvement of the 1H$^+$/1e$^-$ PCET process (eqn (1) below, Fig. S10).

In 9 : 1 CH_3CN : H_2O, the Mn(IV/V) couple was observed at $E_{1/2}$ = 0.66 V *vs.* SCE and CPE at this potential also led to the formation of **2**. Overall, the formation of **2** from **1** is governed by sequential PCET events, as assigned based on the observed redox couples. It is important to note that in both solvents, the Mn(IV/V) redox couple appeared at a close redox potential ($\Delta E_{1/2}$ = 100 mV) (Fig. 5A). The striking 10^4 order enhancement in reactivity upon moving from CH_3CN to water, despite minimal changes in redox potential, unequivocally rules out redox tuning as the predominant driving force.

$$\left[(\text{Ph, Me-bTAML})\text{Mn}^{\text{IV}}(\text{OH})(\text{H}_2\text{O})\right]^- \xrightarrow{1\text{H}^+\ 1\text{e}^-} \left[(\text{Ph, Me-bTAML})\text{Mn}^{\text{III}}(\text{H}_2\text{O}_2)\right]^- \quad (1)$$

$$\left[(\text{Ph, Me-bTAML})\text{Mn}^{\text{V}}(\text{O})\right]^- \xrightarrow{1\text{H}^+\ 1\text{e}^-} \left[(\text{Ph, Me-bTAML})\text{Mn}^{\text{IV}}(\text{OH})(\text{H}_2\text{O})\right]^- \quad (2)$$

Theoretical insight

The reaction pathway was further studied employing density functional theory (DFT) to gain additional insight into the dramatic increase in the reaction rate upon changing the solvent. The computational method is extensively benchmarked against experimental IR and Raman spectra (see SI Section 3 for details). The ground state of the Mn(V)-oxo complex, **2**, is a singlet. The corresponding triplet state is significantly higher in energy, 12 kcal mol^{-1} in CH_3CN and 22 kcal mol^{-1} in water. As the reaction proceeds, however, the triplet state becomes lower in energy than the singlet state. We have captured the minimum energy crossing point (MECP) for the intersection of the two potential energy surfaces (Fig. 6a). Analysis of the partial atomic (Hirshfeld) charges suggests that there is significant charge transfer from BNAH to the metal complex at the MECP (0.7*e* in ACN and 0.8*e* in water). Due to increased polarity, the MECP is more stable in the highly polar solvent water (by ~8 kcal mol^{-1}) with the O-atom bonded to the Mn centre, gaining majority of the excess charge (Fig. 6c). We believe that the striking increase in rate in water as compared to CH_3CN is due

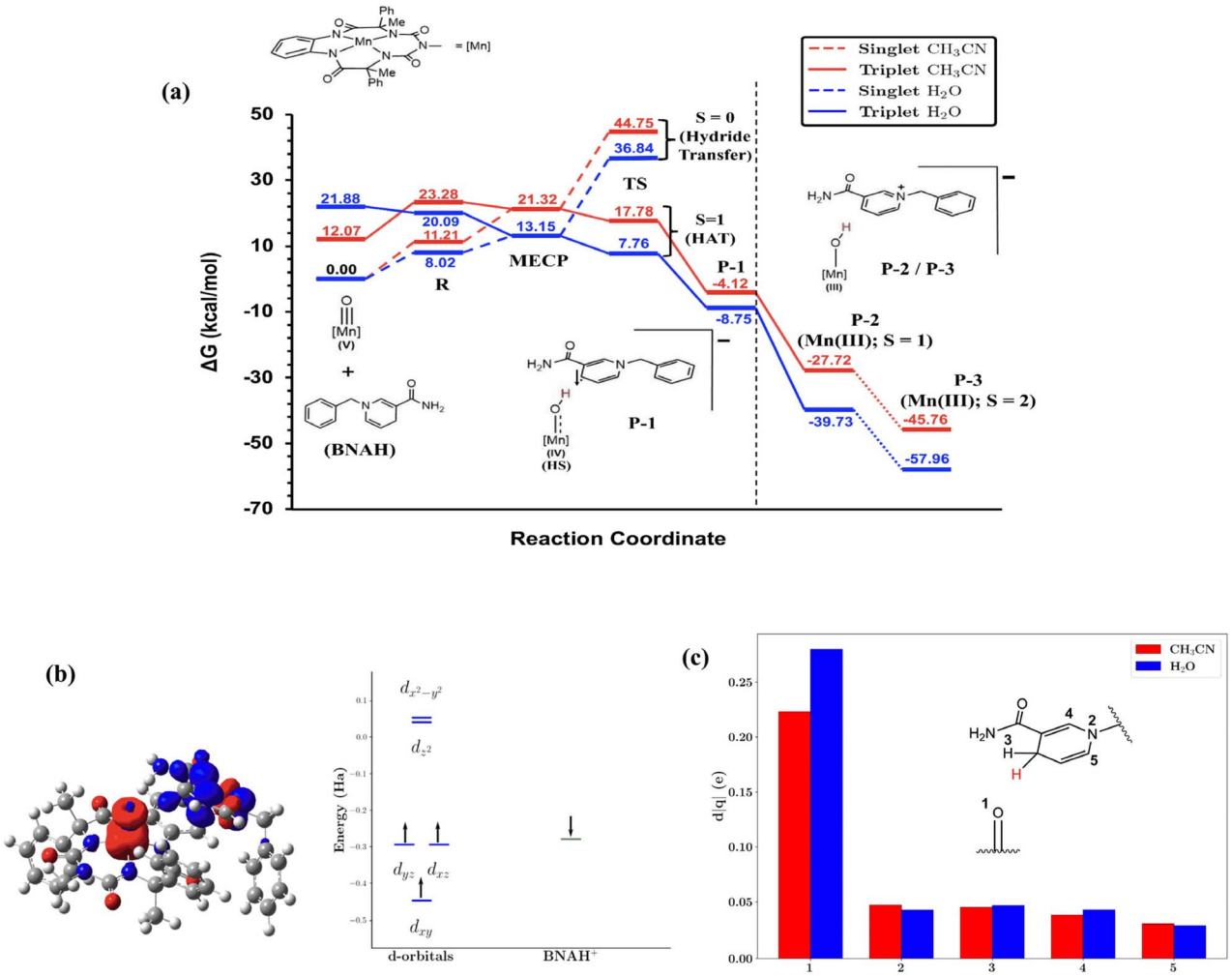

Fig. 6 (a) Mechanism of the net hydride transfer that involves a H-atom transfer from BNAH to the Mn(V)O complex, **2** to generate the triplet P1 state. The system demonstrates a 2-state reactivity where the lowest energy spin configuration of the ground state is a singlet but the transition state is more stable in the triplet configuration. (b) The spin density distribution at the MECP in water; red = alpha and blue = beta; (c) the difference in partial charges on each atom (major contributors) between the MECP and the ground state in water (blue) and acetonitrile (red).

to this differential stabilisation of the MECP, the highest energy point in the reaction path. The sigmoidal behaviour of the rate enhancement, however, is a more subtle issue that cannot be captured accurately by considering the solvent as a dielectric continuum. The nature of dielectric constant dependence of the Born solvation free energy indicates that the gradient of the change in the free energy difference between the MECP and the ground state should decrease with the increase in the dielectric constant of the medium. However, it does not account for the heterogeneity in the water structures at low mole fractions. Moreover, the absolute value of the stabilisation should be considered in a qualitative fashion rather than quantitatively while comparing with the experimental findings because of the approximate way by which the MECP has been calculated. A more accurate calculation would require at least the energy difference between the two spin surfaces to be evaluated at a multi-reference level. Beyond the MECP, the reaction proceeds downhill towards the Mn(IV)O intermediate, P-1, by encompassing the transition state. While the proton is mostly on the reactant side at the MECP, it is almost in between the donor and the acceptor sites at the TS. Since there is no stable intermediate between the MECP and the TS on the triplet surface, the reaction is still supposed to exhibit the KIE, which is characteristic of a PCET reaction.[49,50]

At P-1, a fast electron transfer to the Mn(III)O species gives rise to the P-2 species, which then undergoes a spin-state transformation to the stable high-spin state, P-3. The lowest energy spin-configuration of the intermediate state P-1 can be best described as a high spin Mn(IV) centre that is antiferromagnetically coupled to the BNA radical (Fig. 6b). Note that the higher energy transition state on the singlet surface involves a hydride transfer where the Mn(V) centre in the reactant is directly reduced by two electrons to the low-spin Mn(III) state as shown by the dashed line in Fig. 6a.

OAT reactivity studies of 2 in both media

Since **2** did not react with styrene, oxygen atom transfer (OAT) reactivity was also examined using **2**, which used thioanisole

and triphenylphosphine as substrates. Owing to the substrate solubility problem in water, initial rate calculations under pseudo-first order circumstances were used to compare the kinetic studies in the two media (checking the product formation by GC-MS at different time intervals) at RT (Fig. S26, S27, S33 and Table S10). It was demonstrated that the oxygen atom transfer rate in water was 60 times higher than in an acetonitrile medium using triphenylphosphine as a substrate. The increase in OAT rate was not as large as that of HAT.

Conclusions

Before concluding, it is essential to compare the water-assisted rate enhancement observed for the Mn(V)-oxo bTAML complex with the analogous effects induced by redox inactive metal ions and Lewis or Brønsted acids on other Mn(IV) and Mn(V)-oxo complexes. For instance, coordination of one or two redox inactive metal ions to Mn(IV) or Mn(V)-oxo complexes supported by N_4Py, Bn-TPEN, or TAML ligand frameworks significantly enhances the rates of electron transfer (ET) and oxygen atom transfer (OAT) reactions by modulating redox potentials, while concurrently leading to a decrease in the HAT rate.[28–33] In contrast, the addition of Lewis acids (LAs), such as $Zn(OTf)_2$, $B(C_6F_5)_3$, to the high-valent corrole Mn(V)-oxo complex enhances their HAT reactivity due to their conversion into the Mn(IV)-oxo radical cation valence tautomer.[34] Likewise, treatment of Mn-oxo complexes with Brønsted acids such as triflic acid markedly increases the rates of ET and OAT (up to 10^5-fold) by tuning the redox potential, although the HAT rate for CHD decreases under such conditions.[35–37] However, no previous report has shown HAT rate enhancement in any Mn-oxo complex was achieved solely through solvent modulation or transition into an aqueous medium.

In summary, we report a remarkable water-driven rate enhancement in hydrogen atom transfer (HAT) reactivity using a newly developed non-heme Mn(V)-oxo complex. This complex, thoroughly characterised in terms of structure and properties, is quite stable towards C–H bonds in organic solvents such as acetonitrile. However, its HAT rate towards C–H bonds (<80 kcal mol^{-1}) increases dramatically with increasing water content, reaching a maximum in pure water (up to ~26 000-fold increase in comparison to CH_3CN). Previous studies reported a 60-fold increase in the reaction rate at 70% water content compared to pure CH_3CN for the related $[Fe^V(O)bTAML]^-$ complex,[22] and a 300-fold increase in pure water compared to CH_3CN for the $[Fe^V(O)(Ph,Me\text{-}bTAML)]^-$ complex.[25] For this Mn(V)-oxo complex, the >25 000-fold increase in reactivity in water occurs despite having nearly identical ground-state properties in both water and CH_3CN, such as pK_a and redox potential. This unexpected rate enhancement was attributed to the stabilisation of minimum-energy crossing points (MECPs) in water, facilitated by stronger electrostatic interactions *via* greater partial-charge stabilisation of all atoms in the transition state due to water's higher dielectric constant compared to CH_3CN. Notably, this represents the first example of a non-heme Mn(V)-oxo complex achieving unprecedented rate enhancement solely through solvent modulation, without structural alteration or external additives,[29,36,37,51–56] highlighting water's pivotal role in bioinspired catalysis.

Author contributions

The concept of the work was designed by S. S. G. and P. D. P. D. performed major experiments. K. M. assisted P. D. during CV measurements. S. S. carried out the Raman experiment. S. A. and S. G. performed all DFT calculations. P. D. and S. S. G. analyzed the data and wrote the manuscript. S. S. G. and P. D. thank Prof. Abhishek Dey for his assistance with the Raman measurements and his valuable scientific inputs on this project. All authors have given approval to the final version of the manuscript.

Conflicts of interest

There are no conflicts to declare.

Data availability

CCDC 2377771 and 2378349 contain the supplementary crystallographic data for this paper.[57a,b]

The authors confirm that the data supporting the findings of this study are available within the article [and/or] its supplementary information (SI). Supplementary information is available. See DOI: https://doi.org/10.1039/d5sc06475a.

Acknowledgements

S. S. G. acknowledges MOE-STARS (Grant No. MoE-STARS/STARS-2/2023-0689) and ANRF, New Delhi (Grant No. CRG/2022/007285) for funding. P. D. thanks CSIR for a fellowship. SG acknowledges support of the Department of Atomic Energy, Government of India, under Project Identification No. RTI 4007.

Notes and references

1 F. Gao, H. Chang, J. Li, R. Wang and Y. Gu, *Curr. Opin. Green Sustainable Chem.*, 2023, **40**, 100774.
2 M. Castro-Puyana, M. L. Marina and M. Plaza, *Curr. Opin. Green Sustainable Chem.*, 2017, **5**, 31–36.
3 M. Cortes-Clerget, J. Yu, J. R. A. Kincaid, P. Walde, F. Gallou and B. H. Lipshutz, *Chem. Sci.*, 2021, **12**, 4237–4266.
4 D. C. Rideout and R. Breslow, *J. Am. Chem. Soc.*, 1980, **102**, 7816–7817.
5 F. Franks, *Water: a matrix of life*, Royal Society of Chemistry, 2000.
6 Y. Jung and R. A. Marcus, *J. Am. Chem. Soc.*, 2007, **129**, 5492–5502.
7 Y. Pocker, *Cell. Mol. Life Sci.*, 2000, **57**, 1008–1017.
8 R. Wolfenden and M. J. Snider, *Acc. Chem. Res.*, 2001, **34**, 938–945.
9 V. Sharma, G. Enkavi, I. Vattulainen, T. Róg and M. Wikström, *Proc. Natl. Acad. Sci. U. S. A.*, 2015, **112**, 2040–2045.

10 P. Saura, D. Riepl, D. M. Frey, M. Wikström and V. R. I. Kaila, *Proc. Natl. Acad. Sci. U. S. A.*, 2022, **119**, e2207761119.
11 J. Zhang, Y. I. Yang, L. Yang and Y. Q. Gao, *J. Phys. Chem. B*, 2015, **119**, 14505–14514.
12 A. Stefánsson, S. Arnórsson and Á. E. Sveinbjörnsdóttir, *Chem. Geol.*, 2005, **221**, 289–311.
13 Y. Wang, H. Chen, M. Makino, Y. Shiro, S. Nagano, S. Asamizu, H. Onaka and S. Shaik, *J. Am. Chem. Soc.*, 2009, **131**, 6748–6762.
14 L. Li, J. Wang, C. Zhou, R. Wang and M. Hong, *Green Chem.*, 2011, **13**, 2071–2077.
15 J. J. Gajewski, *Acc. Chem. Res.*, 1997, **30**, 219–225.
16 S. Narayan, J. Muldoon, M. G. Finn, V. V. Fokin, H. C. Kolb and K. B. Sharpless, *Angew. Chem., Int. Ed.*, 2005, **44**, 3275–3279.
17 Y.-M. Tian, W. Silva, R. M. Gschwind and B. König, *Science*, 2024, **383**, 750–756.
18 R. Breslow, *Acc. Chem. Res.*, 1991, **24**, 159–164.
19 T. Shilpa, M. Neetha and G. Anilkumar, *Adv. Synth. Catal.*, 2021, **363**, 1559–1582.
20 M. Ghosh, K. K. Singh, C. Panda, A. Weitz, M. P. Hendrich, T. J. Collins, B. B. Dhar and S. Sen Gupta, *J. Am. Chem. Soc.*, 2014, **136**, 9524–9527.
21 C. Panda, J. Debgupta, D. Díaz Díaz, K. K. Singh, S. Sen Gupta and B. B. Dhar, *J. Am. Chem. Soc.*, 2014, **136**, 12273–12282.
22 K. K. Singh, M. k. Tiwari, M. Ghosh, C. Panda, A. Weitz, M. P. Hendrich, B. B. Dhar, K. Vanka and S. Sen Gupta, *Inorg. Chem.*, 2015, **54**, 1535–1542.
23 K. K. Singh, M. K. Tiwari, B. B. Dhar, K. Vanka and S. Sen Gupta, *Inorg. Chem.*, 2015, **54**, 6112–6121.
24 B. Chandra, P. De and S. Sen Gupta, *Chem. Commun.*, 2020, **56**, 8484–8487.
25 S. Jana, P. De, C. Dey, S. G. Dey, A. Dey and S. S. Gupta, *Chem. Sci.*, 2023, **14**, 10515–10523.
26 R. Gera, P. De, K. K. Singh, S. A. V. Jannuzzi, A. Mohanty, L. Velasco, Kulbir, P. Kumar, J. F. Marco, K. Nagarajan, C. Pecharromán, P. M. Rodríguez-Pascual, S. DeBeer, D. Moonshiram, S. S. Gupta and J. Dasgupta, *J. Am. Chem. Soc.*, 2024, **146**, 21729–21741.
27 T. J. Collins, R. D. Powell, C. Slebodnick and E. S. Uffelman, *J. Am. Chem. Soc.*, 1990, **112**, 899–901.
28 H. Yoon, Y. M. Lee, X. Wu, K. B. Cho, R. Sarangi, W. Nam and S. Fukuzumi, *J. Am. Chem. Soc.*, 2013, **135**, 9186–9194.
29 S. Hong, Y. M. Lee, M. Sankaralingam, A. K. Vardhaman, Y. J. Park, K. B. Cho, T. Ogura, R. Sarangi, S. Fukuzumi and W. Nam, *J. Am. Chem. Soc.*, 2016, **138**, 8523–8532.
30 C. G. Miller, S. W. Gordon-Wylie, C. P. Horwitz, S. A. Strazisar, D. K. Peraino, G. R. Clark, S. T. Weintraub and T. J. Collins, *J. Am. Chem. Soc.*, 1998, **120**, 11540–11541.
31 L. Dong, Y. Wang, Y. Lv, Z. Chen, F. Mei, H. Xiong and G. Yin, *Inorg. Chem.*, 2013, **52**, 5418–5427.
32 W. W. Lam, S.-M. Yiu, J. M. Lee, S. K. Yau, H.-K. Kwong, T.-C. Lau, D. Liu and Z. Lin, *J. Am. Chem. Soc.*, 2006, **128**, 2851–2858.
33 J. Chen, Y.-M. Lee, K. M. Davis, X. Wu, M. S. Seo, K.-B. Cho, H. Yoon, Y. J. Park, S. Fukuzumi, Y. N. Pushkar and W. Nam, *J. Am. Chem. Soc.*, 2013, **135**, 6388–6391.
34 R. A. Baglia, C. M. Krest, T. Yang, P. Leeladee and D. P. Goldberg, *Inorg. Chem.*, 2016, **55**, 10800–10809.
35 D. G. Karmalkar, M. S. Seo, Y.-M. Lee, Y. Kim, E. Lee, R. Sarangi, S. Fukuzumi and W. Nam, *Inorg. Chem.*, 2021, **60**, 16996–17007.
36 J. Chen, H. Yoon, Y.-M. Lee, M. S. Seo, R. Sarangi, S. Fukuzumi and W. Nam, *Chem. Sci.*, 2015, **6**, 3624–3632.
37 Y.-M. Lee, S. Kim, K. Ohkubo, K.-H. Kim, W. Nam and S. Fukuzumi, *J. Am. Chem. Soc.*, 2019, **141**, 2614–2622.
38 K. Barbara Schowen, R. L. Schowen and D. L. Purich, *Methods Enzymol.*, 1982, **87**, 551–606.
39 J. P. Roth and J. M. Mayer, *Inorg. Chem.*, 1999, **38**, 2760–2761.
40 J. R. Bryant and J. M. Mayer, *J. Am. Chem. Soc.*, 2003, **125**, 10351–10361.
41 W. W. Y. Lam, W.-L. Man and T.-C. Lau, *Coord. Chem. Rev.*, 2007, **251**, 2238–2252.
42 A. Davidović, I. Tabaković, D. Sladić, N. Dogović and M. J. Gašic, *J. Electroanal. Chem. Interfacial Electrochem.*, 1991, **321**, 457–468.
43 R. G. Agarwal, S. C. Coste, B. D. Groff, A. M. Heuer, H. Noh, G. A. Parada, C. F. Wise, E. M. Nichols, J. J. Warren and J. M. Mayer, *Chem. Rev.*, 2022, **122**, 1–49.
44 S. Fukuzumi, H. Kotani, K. A. Prokop and D. P. Goldberg, *J. Am. Chem. Soc.*, 2011, **133**, 1859–1869.
45 M. H. V. Huynh and T. J. Meyer, *Chem. Rev.*, 2007, **107**, 5004–5064.
46 D. R. Weinberg, C. J. Gagliardi, J. F. Hull, C. F. Murphy, C. A. Kent, B. C. Westlake, A. Paul, D. H. Ess, D. G. McCafferty and T. J. Meyer, *Chem. Rev.*, 2012, **112**, 4016–4093.
47 C. Costentin, M. Robert and J.-M. Savéant, *Chem. Rev.*, 2010, **110**, PR1–PR40.
48 L. Zhang, X. Jiang, E. Wang and S. Dong, *Biosens. Bioelectron.*, 2005, **21**, 337–345.
49 J.-H. Chen, W.-T. Li, K.-Y. Cai, H.-J. Tu, Z.-T. Long, S. Akhtar and L.-D. Liu, *Nat. Commun.*, 2025, **16**, 3789–3800.
50 S. Hammes-Schiffer, *Acc. Chem. Res.*, 2025, **58**, 1335–1344.
51 J. Park, Y. Morimoto, Y.-M. Lee, W. Nam and S. Fukuzumi, *J. Am. Chem. Soc.*, 2012, **134**, 3903–3911.
52 S.-S. Xue, X.-X. Li, Y.-M. Lee, M. S. Seo, Y. Kim, S. Yanagisawa, M. Kubo, Y.-K. Jeon, W.-S. Kim, R. Sarangi, S. H. Kim, S. Fukuzumi and W. Nam, *J. Am. Chem. Soc.*, 2020, **142**, 15305–15319.
53 A. H. Reath, J. W. Ziller, C. Tsay, A. J. Ryan and J. Y. Yang, *Inorg. Chem.*, 2017, **56**, 3713–3718.
54 A. M. Zima, O. Y. Lyakin, A. A. Bryliakova, D. E. Babushkin, K. P. Bryliakov and E. P. Talsi, *Catalysts*, 2022, **12**, 949–963.
55 J. K. Satpathy, R. Yadav, U. K. Bagha, D. Kumar, C. V. Sastri and S. P. de Visser, *Inorg. Chem.*, 2024, **63**, 6752–6766.
56 A. Das, N. Pal, J. Xiong, V. G. Young Jr, Y. Guo, M. Swart and L. Que Jr, *J. Am. Chem. Soc.*, 2025, **147**, 292–304.
57 (*a*) CCDC 2377771: Experimental Crystal Structure Determination, 2025, DOI: 10.5517/ccdc.csd.cc2kt89z; (*b*) CCDC 2378349: Experimental Crystal Structure Determination, 2025, DOI: 10.5517/ccdc.csd.cc2ktvy6.